End-to-End Differentiable Force Field Generator with Crystal Structure Differentiation and Matching

Hiroshi Nakano, Shinnosuke Hattori, Hajime Kobayashi, Takumi Araki, Masakazu Ukita, Toshio Nishi, Yoshihiro Kudo

Material and Device Analysis Center, Sony Semiconductor Solutions Corporation
4-14-1, Asahi-cho, Atsugi, Kanagawa, Japan

KEYWORDS: automatic differentiation, crystal structure, differentiable programming, force field, implicit function theorem, organic molecule.

Abstract

In this paper, we introduce a novel approach for force field (FF) parameterization, called structure differentiation and matching (SDM), which leverages direct matching of crystal structures and atomic charges optimization in an end-to-end differentiable manner. Traditional FF parameterization methods have been accelerated by differentiable programming and automatic differentiation (AD), enabling energy and force matching through force differentiation and matching (FDM). However, crystal structure matching with AD remains challenging due to the difficulty of differentiation of converged structures optimized by iterative algorithms with respect to FF parameters. To address this limitation, we propose SDM, which incorporates reference data such as stable monomer structures, crystal structures, lattice energies, and potential energy surfaces (PESs) of dihedral angles. SDM utilizes implicit function differentiation (IFD) and differentiable Ewald techniques to optimize FF parameters and atomic charges simultaneously. We demonstrate the effectiveness of SDM through a case study involving eight exemplified molecules, showing significant improvements over conventional FDM with error factors reduced to less than one-quarter when using the SDM (q-opt) charge optimization method. SDM achieves high precision in reproducing lattice constants, atomic configurations, lattice energies, and PESs. Molecular dynamics simulations further confirm the stability of the generated crystal structures. SDM can be extended to other FF categories, such as polarized FFs and those with explicit hydrogen bonding interactions. We anticipate that SDM (q-opt) will emerge as a standard method for FF parameterization using crystal structures, offering a promising avenue for advancing the field of molecular simulations.

1. Introduction

Molecular dynamics (MD) is a pivotal tool in the field of atomic and molecular modeling, particularly for small organic molecules.[1–3] It plays a crucial role in structure-based drug design, where characterization of intermolecular interactions is essential for predicting ligand activity.[4–7] Additionally, MD provides invaluable insights into the fundamental mechanisms governing the condensed matter properties of a wide range of materials.[8–10] Moreover, MD is also indispensable in studies involving quantum mechanics/molecular mechanics (QM/MM), where it is used to create a realistic MM region for accurate simulations.[11–19]

The accuracy of MD simulations relies on three key factors: the type of force fields (FFs) employed, the reference data used, and the FF optimization algorithms employed. FFs can be categorized into classical FFs, such as the generalized Amber force field (GAFF)[20–22] and neural network potentials (NNPs)[23–39], which have gained attention in recent years. While NNPs have shown promise, classical FFs remain interpretable and advantageous due to their simple equations and fewer parameters.[20–22] Therefore, this study specifically focuses on classical FFs.

The reference data for generating FFs can be obtained from either QM calculations or experimental data.[36] In the case of experimental data, there is active research in FF optimization techniques aimed at reproducing measurable physical properties.[36,40,41] One of the critical experimental datasets used for this purpose is the crystal structure obtained from single-crystal X-ray diffraction, particularly for small organic molecules as it contains intermolecular structure data. Crystal structure reproducibility has been widely used to validate FFs,[42–44] and cohesive properties such as lattice energy have been employed to assess the stability or strength of intermolecular interactions.[45–47] These crystal structures are typically compiled in the Cambridge Structural Database (CSD), and data on sublimation enthalpies, which can be converted to lattice energies, are also readily accessible.[48] It is important not only to reproduce crystal structures and cohesive energy, but also to reproduce other material properties relevant to their intended use. However, reproducing these two factors is often a prerequisite for reproducing subsequent material properties. Therefore, our focus is on the development of FF generation techniques that can accurately reproduce crystal structures and lattice energies.

The optimization algorithms for FFs can be classified into two categories: non-differentiating and differentiating methods. Well-known MD software packages such as Assisted Model Building with Energy Refinement (AMBER)[1] and Chemistry at Harvard Macromolecular Mechanics (CHARMM)[3] groups have developed original FFs, but further optimizations have been performed. Non-differentiating algorithms include Bayesian optimization methods,[49–53] evolutionary algorithms,[54] and particle swarm optimization[55,56], while differentiating methods involve optimization algorithms that contain derivative coefficients to differentiate a function evaluating the FFs. These coefficients enable efficient optimization for numerous variables, such as gradient descent methods or quasi-Newton methods. For example, a software package called ForceBalance has been developed to generate FFs using numerical differentiation.[22,40,41,57–60] More recently, several methods based on automatic differentiation (AD) have been proposed to mitigate approximation errors and improve the efficiency of derivative calculations.[61–65] Therefore, in this study, we focused on AD-based FF generation techniques.

However, generating FFs with reference to crystal structures poses challenges because crystal structures do not provide information on the energies and forces acting on atoms. The only information obtainable from crystal structures is whether the structure is stable compared to its surrounding structures. In contrast, the energy and force information of various structures, which are required as training data in NNPs and conventional differentiable FF parameterizations, cannot be solely obtained from crystal structures.[23–39,45,65] Although the energy and force of structures near the crystal structure can be evaluated using quantum mechanical calculations, the comprehensive calculation of forces in unstable structures becomes computationally expensive due to the requirement of highly accurate intermolecular interactions. Moreover, FF optimization with AD has certain limitations when using crystal structures as the reference data. The crystal structures were evaluated using an iterative structure-optimization algorithm to converge the forces to zero. However, the convergence structures cannot be automatically differentiated with the FF parameters due to the chain rule of differentiation in AD, which continuously connects all the iterations to each other. This forms an immensely deep network structure that requires extensive memory and renders the optimization unstable.[36,63,66]

The available information from crystal structures is limited to the fact that the forces acting on each atom are balanced to zero. The calculation of forces using FFs follows a deterministic algorithm, which allows for the computation of derivative coefficients of forces on the atoms with respect to FF parameters. In this paper, this method is denoted as force differentiation and matching (FDM). However, the optimization goal of achieving zero forces at the experimental crystal structures may not necessarily align with the true objective of accurately reproducing the experimental structures. Unlike NNPs, the optimization of classical FFs is an overdetermined problem, where there are fewer parameters than equations for reproducing the reference data. Therefore, as achieving zero forces at the reference structures is generally impossible, FFs generated with FDM may not ensure that the optimized crystal structures or monomer structures with the FFs are close to the reference structures.

To address this limitation, we propose a method based on implicit function differentiation (IFD) to differentiate the converged crystal structures of the iterative algorithms with respect to FF parameters.[66] This approach, called structure differentiation and matching (SDM), uses the derivative coefficients to optimize FF parameters, ensuring correspondence between experimental and converged structures using FFs. SDM develops an automatic FF generation program that utilizes reference data such as stable single-molecule structures, crystal structures, crystallization energy, and potential energy surfaces (PESs) of free rotating dihedral angles. By leveraging IFD, SDM offers a more robust and accurate approach to FF optimization compared to FDM, allowing for improved alignment between FF-optimized structures and experimental reference data.

In addition, considering long-range Coulombic interactions is crucial when creating FFs using crystal structures as a reference. Therefore, it is desirable to implement the Ewald method in a differentiable form, allowing for atomic charge optimization as one of the FF parameters. [67]

In our case study, we compare four methods: FDM and SDM, each with and without atomic charge optimization using the differentiable Ewald method. We evaluate the performance of these methods on eight different materials, including anthracene, biphenyl, and benzoic acid. The optimized FF parameters can be output in Large-scale Atomic/Molecular Massively Parallel Simulator (LAMMPS) form,[2] demonstrating consistency between the proposed program and LAMMPS, with errors below 1.0×10^{-3} kcal/mol. As a result, the FFs generated by our proposed program are readily applicable for large-scale MD simulations using LAMMPS, offering improved accuracy and reliability in simulating the behavior of materials at the atomic level.

2. Methodology

2.1. Force Field

We used AMBER-type FFs to ensure compatibility with the existing MD software,[1,2] The FFs are expressed as

$$E_{\text{total}} = E_{\text{bond}} + E_{\text{angle}} + E_{\text{dihed}} + E_{\text{vdw}} + E_{\text{coul}} \tag{1}$$

$$E_{\text{bond}} = \sum_{\text{bond } r} K_r \left(r - r_{\text{eq}}\right)^2, \tag{2}$$

$$E_{\text{angle}} = \sum_{\text{angle } \theta} K_\theta \left(\theta - \theta_{\text{eq}}\right)^2, \tag{3}$$

$$E_{\text{dihed}} = \sum_{\text{dihed } \phi} \sum_{n=1}^{4} \frac{V_n}{2} \left[1 + \cos(n\phi - \gamma_n)\right], \tag{4}$$

$$E_{\text{vdW}} = \sum_{i<j} 4\epsilon \left[\left(\frac{\sigma_{ij}}{r_{ij}}\right)^{12} - \left(\frac{\sigma_{ij}}{r_{ij}}\right)^{6}\right], \tag{5}$$

$$E_{\text{coulomb}} = \sum_{i<j} \frac{q_i q_j}{\epsilon_p r_{ij}}. \tag{6}$$

The total energy of the system, denoted as E_{total}, is composed of several components, including bond energy (E_{bond}), angular energy (E_{angle}), dihedral angular energy (E_{dihed}), van der Waals (vdW) force potential (E_{vdW}) in the Lenard-Jones (LJ) form, and Coulomb potential (E_{coul}). The optimization of FFs involves optimizing a set of variables shown in **Table 1**, denoted as vector **p**. The dihedral angle parameter, γ_n, is set to either 0 or π, as the same conformational space can be explored by optimizing the V_n parameter. We used the coefficients from Open Force Field v 1.0.0[22] for consistency, and the charge coefficient, q, was set to 0.1 e (elementary charge) to ensure comparability with other variables. Additionally, a constraint condition was imposed to ensure that the sum of charges was zero for each molecule.

To improve optimization accuracy through differentiation methods, we included as many types of vdW parameters and atomic charges as possible, considering molecular symmetry.[49–56] This is based on the concept of equivariance, which accounts for translational and rotational symmetry, and extends to equivalent atoms on molecular graphs. As an example, benzoic acid (BENZAC) is presented in **Figure 1**. In total, we selected 11 types of atoms, denoted as C1 to C5, H1 to H4, O1, and O2, and generated 22 vdW parameters and 11 atomic charges, providing a higher degree of freedom to the FFs. The LJ parameters for different atom types were generated using arithmetic mixing, following established methods.[1,2,21]

In MD simulations of crystal structures using a periodic system, it is crucial to account for the long-range interactions arising from the Coulomb potential. Atomic charges are also important parameters that characterize both intra- and intermolecular interactions. To optimize these FF parameters, including atomic charges, we implemented a differentiable Ewald method. While the particle mesh Ewald (PME) method is commonly used due to its lower computational cost compared to the Ewald method [68], our objective was to introduce a new approach for FF construction that accurately reproduces small molecule crystal structures. The FFs were primarily evaluated for a unit lattice, without exploring larger systems, which limits the advantages of the PME method to small-sized molecules. Therefore, we employed the theoretically simpler Ewald method [67], which is expressed as:

$$E_{\mathrm{coulomb}} = E^{S} + E^{L} - E^{\mathrm{self}}, \tag{7}$$

$$E^{S} = \frac{1}{2\epsilon_p} \sum_{\boldsymbol{n}} \sum_{i=1}^{N} \sum_{j=1, j\neq i}^{N} \frac{q_i q_j}{\left|r_{ij} + \boldsymbol{n}\cdot\boldsymbol{L}\right|} \operatorname{erfc}\left(\frac{\left|r_{ij} + \boldsymbol{n}\cdot\boldsymbol{L}\right|}{\sqrt{2\sigma}}\right), \tag{8}$$

$$E^{L} = \frac{2\pi}{V\epsilon_p}\sum_{k\neq 0}\frac{\mathrm{e}^{-\sigma^2 \mathrm{k}^2/2}}{k^2}|S(\boldsymbol{k})|^2 , \tag{9}$$

$$E^{\mathrm{self}} = \frac{1}{\epsilon_p}\frac{1}{\sqrt{2\pi}\sigma}\sum_{i=1}^{N} q_i^2 , \tag{10}$$

where n, $\boldsymbol{L}$, $\boldsymbol{k}$, and $S(\boldsymbol{k})$ represent a natural number vector, lattice vector, reciprocal lattice vector, and structure factor of the lattice, respectively, and the constant σ balances the short- and long-range terms. The appropriate coefficient must be multiplied to match the other energy terms.

To ensure seamless integration with LAMMPS, we have implemented neighbor lists and special bonds in our program. Additionally, we applied a CHARMM-style energy-switching function to E_{vdW}[3,69], using the LAMMPS keyword "lj/charmm/coul/long" for non-bonding interactions. The remaining parameters, such as the dielectric constant (ϵ_p) and the distance threshold for accounting Coulomb and LJ potentials for atoms within three topological distances (special bonds), were kept constant. We set the dielectric permittivity (ϵ_p) to 3.0 and used DREIDING type for special bonds, while the parameters for the improper type of dihedral angles were set to the same values as GAFF.[20,21] Notably, the energies calculated by our program for all tested molecules were in excellent agreement with those obtained from LAMMPS, with errors below 1.0×10^{-3}. Moreover, our program is capable of outputting FFs in the LAMMPS format, providing added convenience.[2]

Table 1. Regularization factors in FF optimization. The factors were used in evaluation functions minimized with the differentiation-based optimization algorithms SDM and FDM.

Type	Regularization factor
bond force constant K_r	100 kcal/mol/Å^2
equilibrium bond length r_{eq}	0.1 Å
angle force constant K_θ	100 kcal/mol^{-1} rad^2
equilibrium angle θ_{eq}	20 degrees
dihedral force constant V_n	1 kcal/mol
vdW well depth ϵ	0.1 kcal/mol
vdW length σ	1 Å
charge q	0.1 e

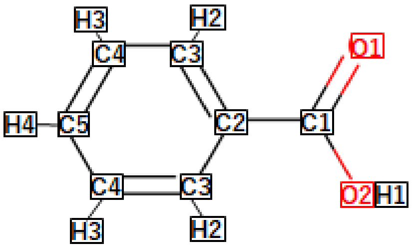

Figure 1: Symmetry-based atom type assignment. In GAFF, the original atom type assignment treats H2, H3, and H4, as well as C3, C3, C4, and C5, as equal types. The number of atom types is increased based on the graph symmetry, which considers equivalent atoms.

2.2. Evaluation Function

In this study, our FF optimization approach involved multiple evaluation functions: (i) an evaluation function (L^M) for the monomer structure, (ii) a crystal structure evaluation function (L^C), (iii) an evaluation function for the lattice energy (L^E), and (iv) PES evaluation functions (L_l^P) for dihedral angle *l* of freely rotating bonds. Since a molecule may have multiple dihedral angles, the evaluation function for PESs can be expressed as the summation of the corresponding terms. The definition of the evaluation function is as follows:

$$L^{all} = w^M L^M + w^C L^C + w^E L^E + \sum_l w_l^P L_l^P \,, \tag{11}$$

where w^{M}, w^{C}, w^{E}, and w_l^{P} denote the weights balancing the corresponding terms. To enhance the accuracy of a specific evaluation item, we can adjust the weights based on the research objective. The values and reasons for these weights in our study are detailed in **Table S1**. Additionally, we imposed a constraint that ensures the sum of charges of atoms in a molecule equals the total charge Q, which was set to zero as all selected molecules were neutral. To confine the search ranges within physically reasonable values, we employed constraints defined by inequalities, as described in **Table S2**. To optimize the FF parameters with these constraints, inequality relations, and gradients, we utilized the sequential least-squares programming (SLSQP) optimization method with SciPy [70]. The four terms in Eq. (11) are explained below.

2.2.1. Evaluation function for single molecule structures

The evaluation function L^{M} quantifies the deviation between the reference single molecule structure and the converged structure optimized with a FF. The optimization was performed using the gradient descent method in JAXOPT.[71] To compare the structures, we utilized internal coordinates $\mathbf{u}_M = (\boldsymbol{r}, \boldsymbol{\theta}, \boldsymbol{\phi})$ instead of cartesian coordinates $\mathbf{u}$, where $\boldsymbol{r}$ denotes the bond length, $\boldsymbol{\theta}$ indicates the bond angle, and $\boldsymbol{\phi}$ represents the dihedral angle. The regularization coefficients for $\boldsymbol{r}_{\mathrm{eq}}$ in **Table 1** were multiplied by the value of $\boldsymbol{r}$, and the coefficients of $\boldsymbol{\theta}_{eq}$ were also multiplied by both $\boldsymbol{\theta}$ and $\boldsymbol{\phi}$, to adjust the units and ensure they are defined as belonging to a vector $\mathbf{u}_{\mathrm{M}}$. This approach allows for equivalent impact on the evaluation function L^M for a bond length variation of 0.1 Å and an angular difference of 20°.[22] The internal coordinates are symmetric for translational and rotational operations, and the AMBER-type FF is expressed in a form that assumes internal coordinates as arguments, making them suitable for evaluating the structural similarity of individual molecules. The reference structure is denoted as $\mathbf{u}'_{\mathrm{M}}$, and the structure optimized with FF is denoted as $\tilde{\mathbf{u}}_{\mathrm{M}}$. In the following sentences, the prime symbol indicates reference data and the tilde indicates a structure calculated with an FF. The evaluation function for single molecule structures can be expressed as

$$L^{\mathrm{M}} = (\tilde{\mathbf{u}}_{\mathrm{M}}(\mathbf{p}) - \mathbf{u}'_{\mathrm{M}})^2. \tag{12}$$

2.2.2. Evaluation function for crystal structures

For crystal structure matching, lattice vector matching as well as the atomic coordinates are required. The evaluation function is defined as

$$L^{\mathrm{C}} = (\tilde{\mathbf{u}} - \mathbf{u}')^2 + c_{\mathrm{L}}\left(\tilde{\boldsymbol{T}}_v - \boldsymbol{T}'_v\right)^2, \tag{13}$$

where $\tilde{\boldsymbol{T}}_v$ denotes three lattice vectors in the converged structures and T'_v is that in the reference structures. The coefficient c_{L}, which defines the importance of lattice vectors compared to internal atomic coordinates, was set to 10 to account for the fact that variations in the lattice vector $\boldsymbol{T}_v$ can influence all atoms in the crystal and should be considered more essential than a coordinate of an individual atom. In crystal structure matching, the equivalency for rotation and translational symmetries is not necessary, as crystal lattices induce a loss of symmetries. Therefore, the similarity of crystal structures was compared in terms of cartesian coordinates. To represent the extended coordinates, we used $\tilde{\mathbf{u}}_{\mathrm{C}} = \left(\tilde{\mathbf{u}}^T, \tilde{T}_v^T\right)^T$, where T denotes transpose, to incorporate both the internal coordinates and lattice vectors.

2.2.3. Evaluation function for lattice energy

The lattice energy U'_{lat} was computed from the experimental accessible values of the sublimation enthalpy H_{subl} that is correlated with the lattice energy as

$$H_{\mathrm{subl}} = -U'_{\mathrm{lat}} - 2RT \; , \tag{14}$$

where R denotes the gas constant and T indicates the temperature.[48] Based on the crystal structure energy per unit cell E^{C} and the single molecule energy E^{M}, the lattice energy $\widetilde{U}_{\mathrm{lat}}$ can also be defined as follows:

$$\widetilde{U}_{\mathrm{lat}} = E^{\mathrm{M}} - \frac{E^{\mathrm{C}}}{N_{\mathrm{mol}}} \, . \tag{15}$$

The evaluation function for the lattice energy matching L^{E} can be evaluated as follows:

$$L^{E} = \left(\widetilde{U}_{lat}(\tilde{\mathbf{u}}_C, \mathbf{p}) - U'_{\mathrm{lat}}\right)^2 . \tag{16}$$

An FF reproducing both the crystal structure and the lattice energy U_{lat}, enables the simulation of MD with the FF to reflect the stability of the crystal. [48]

2.2.4. Evaluation function of PESs

The total evaluation function should include the evaluation functions for matching PES of freely rotatable dihedral angles. The reference data were acquired with the QM calculation of a single molecule. The evaluation functions of the energy surface PES along with the rotation of the dihedral angles *l* can be defined as:

$$L_l^{\mathrm{P}} = \sum_{\boldsymbol{u} \in \mathrm{PES}_l} \exp\left(-\min\left(E(\mathbf{u},\mathbf{p}), E'(\boldsymbol{u})\right)/2k_B T_{\mathrm{PES}}\right)\left(E(\mathbf{u},\mathbf{p}) - E'(\mathbf{u})\right)^2, \tag{17}$$

where the term $\exp\left(-\min\left(E(\mathbf{u},\mathbf{p}), E'(\mathbf{u})\right)/2k_B T_{\mathrm{PES}}\right)$ includes the coefficients for prioritizing the points near the lowest points in the PES. k_B denotes the Boltzmann constant, and T_{PES} represents the virtual temperature for prioritization, which was set to 2000 K according to ref. [22]. Additionally, to prevent overflow and instability of the L_l^{P} value during the initial stage of the optimization process, we implement a log-damp function. In this function, L_l^{P} is changed to $log(L_l^{\mathrm{P}}) + 1.0$ when its value exceeds 1.0.

2.3. FF optimization methods

2.3.1. Stable structure Differentiation (SDM)

SDM calculates the derivative coefficients of the evaluation function (Eq. (11)) by directly differentiating the stable structures obtained through an iterative optimization algorithm. **Figure 2** depicts the block diagrams of SDM for computing and differentiating L^C, L^M, and L^E. The energy of the systems evaluated using an Amber-type energy function formula (Eq. (1)) with substituted $\tilde{\mathbf{u}}$ and $\mathbf{p}$ is shown in **Figure 2(a)**. The block diagram for differentiating the stable structures with respect to $\mathbf{p}$ is illustrated in **Figure 2(b)**. In the top block, the iterative process was performed to obtain $\tilde{\mathbf{u}}$ using the block defined in **Figure 2(a)**. In conventional implementations, AD was repeated with the same number of iterations for convergence (typically a hundred times) and each iteration included the large number of derivatives of short-range Coulomb potentials E^S (typically more than 10,000) registered in the neighborhood list and other terms in Eq. (1). Therefore, the conventional AD implementations with one hundred layers are computationally intractable. [36] In contrast, the proposed SDM allows for efficient computation of the derivatives. First, the converged structure $\tilde{\mathbf{u}}$ satisfies

$$\boldsymbol{F}(\tilde{\mathbf{u}}(\mathbf{p}), \mathbf{p}) \equiv \frac{\partial E(\tilde{\mathbf{u}}(\mathbf{p}), \mathbf{p})}{\partial \mathbf{u}} = 0\,. \tag{18}$$

Subsequently, both sides of Eq. (18) were differentiated with respect to $\mathbf{p}$ to obtain the following expression:

$$\frac{\partial \boldsymbol{F}(\tilde{\mathbf{u}}, \mathbf{p})}{\partial \mathbf{p}} = \frac{\partial \boldsymbol{F}(\tilde{\mathbf{u}}, \mathbf{p})}{\partial \mathbf{u}} \frac{\partial \mathbf{u}}{\partial \mathbf{p}} + \frac{\partial \boldsymbol{F}(\tilde{\mathbf{u}}, \mathbf{p})}{\partial \mathbf{p}} = 0\,. \tag{19}$$

Replacing $\boldsymbol{F}$ with $\boldsymbol{E}$ yields

$$\frac{\partial^2 E(\tilde{\mathbf{u}},\mathbf{p})}{\partial \mathbf{u}^2}\frac{\partial \mathbf{u}}{\partial \mathbf{p}}+\frac{\partial^2 E(\tilde{\mathbf{u}},\mathbf{p})}{\partial \boldsymbol{u}\partial \mathbf{p}}=0\,, \tag{20}$$

where $\partial^2 E(\tilde{\mathbf{u}},\mathbf{p})/\partial \mathbf{u}^2$ represents the Hessian defined as the second-order differentiation based on the atomic coordinates $\mathbf{u}$. The multiplication of the inverse matrix to both sides of Eq. (20) yields

$$\frac{\partial \tilde{\mathbf{u}}}{\partial \mathbf{p}}=-\frac{\partial^2 E(\tilde{\mathbf{u}},\mathbf{p})}{\partial \mathbf{u}^2}^{-1}\frac{\partial^2 E(\tilde{\mathbf{u}},\mathbf{p})}{\partial \mathbf{u}\partial \mathbf{p}}. \tag{21}$$

While $\tilde{\mathbf{u}}$ can be calculated using an iterative process, the differentiation of $\tilde{\mathbf{u}}$ with SDM does not have to be iterative, as expressed in Eq. (21), and can be computed using a deterministic process. The top block labeled $\tilde{\mathbf{u}}(p)$ in **Figure 2(b)** performs the iterative structure optimization process to obtain $\tilde{\mathbf{u}}$, based on the block diagram shown in **Figure 2(a)**. The bottom block then performs the non-iterative differentiation with respect to $\tilde{\mathbf{u}}$. In Eq. (21), the second term represents the differentiation of $\mathbf{F}$ with respect to $\mathbf{p}$ at $\mathbf{u}=\tilde{\mathbf{u}}$, and the first term replaces the derivative variable from $\mathbf{p}$ to $\mathbf{u}$. Since the dimension of $\mathbf{p}$ is smaller or comparable to that of $\mathbf{u}$, the first term does not significantly impact the computation costs. The inverse matrix calculation also does not pose a significant impact. Overall, the IFD method facilitates the computation of $\partial\tilde{\mathbf{u}}/\partial\mathbf{p}$ with a similar computational cost as a single Hessian $\partial^2 E(\tilde{\mathbf{u}},\mathbf{p})/\partial \mathbf{u}^2$ calculation. As depicted in **Figure 2(c)** and **Figure 2(d)**, $\partial\tilde{\mathbf{u}}/\partial\mathbf{p}$ is embedded in the calculation and differentiation of L^{X} $(\mathrm{X}=\mathrm{M},\mathrm{C})$, and L^{E}.

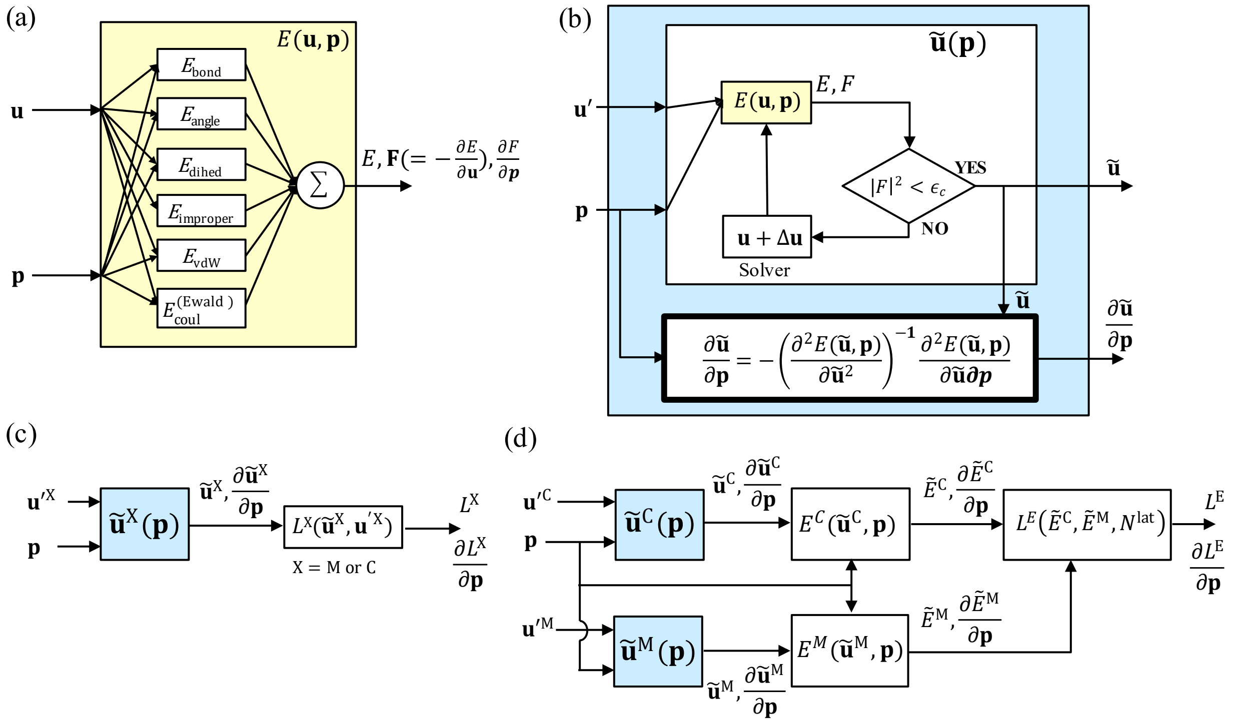

Figure 2: (a) Block diagram illustrating the energy calculation and its differentiation, (b) Block diagram showing the structure optimization and its derivatives with IFD in SDM. $E(\mathbf{u},\mathbf{p})$ in (a) is included in the diagram (b). ϵ_C represents the convergence criterion, and $\Delta\mathbf{u}$ indicates the updates of $\mathbf{u}$. In the bottom block with bold lines, the derivative coefficient $\partial\tilde{\mathbf{u}}/\partial\mathbf{p}$ can be computed using the converged structure $\tilde{\mathbf{u}}$ optimized in the top block with IFT. (c) Block diagram illustrating the partial evaluation functions of L^X (X = M,C). (d) Block diagram illustrating the partial evaluation function of L^E. Differentiation of the function requires two derivative coefficients of $\tilde{\mathbf{u}}^M(\mathbf{p})$ and $\tilde{\mathbf{u}}^C(\mathbf{p})$.

2.3.2. Force Differentiation and Matching (FDM)

FDM optimizes FF by differentiating the forces on the atoms with respect to $\mathbf{p}$. In NNP, it is common to use the method of matching energies and forces obtained from QM calculation.[23–39,45,65]

However, in this study, due to the prerequisite of using only stable structures as reference data, previous studies considering energies and forces for non-stable structures[61–65] are not used. Instead, FDM utilizes only the condition $\boldsymbol{F}(\mathbf{u}', \mathbf{p}) = 0$ at the reference structure $\mathbf{u}'$, which replaces L^{M}, L^{C}, and L^{E} in the following derivation.

$$L^{\mathrm{M,FDM}} = |\boldsymbol{F}^{\mathrm{M}}(\mathbf{u}', \mathbf{p})|^2 , \tag{22}$$

$$L^{\mathrm{C,FDM}} = \left|\boldsymbol{F}^{\mathrm{C}}(\mathbf{u}', \mathbf{p})\right|^2 , \tag{23}$$

$$L^{E,FDM} = \left(\widetilde{U}_{lat}\left(\mathbf{u}'^{C}, \mathbf{p}\right) - U'_{\mathrm{lat}}\right)^2 . \tag{24}$$

$L^{\mathrm{M,\,FDM}}$ and $L^{\mathrm{C,\,FDM}}$ reduce the forces on an atom at the reference structures as zero. The crystal structure $\mathbf{u}'^{C}$ is used in Eq. (24) because FDM cannot differentiate functions involving the converged structures $\widetilde{\mathbf{u}}^{\mathrm{C}}$. In summary, the evaluation function of FDM is defined as

$$L_{FDM}^{all} = w^{M,FDM} L^{M,FDM} + w^{C,FDM} L^{C,FDM} + w^{E} L^{E,FDM} + \sum_{l} w_l^P L_l^P . \tag{25}$$

2.4. Details on Comparative Study of Optimization Methods

The objectives of this study are to compare the accuracy of FFs optimized using FDM and SDM, and to evaluate the accuracy of FFs when combined with a differentiable Ewald method for charge optimization. We assess FFs for each of FDM and SDM under two conditions: keeping charges fixed at their initial values without optimization (q-fix) and optimizing charges along with other parameters (q-opt). We refer to the four optimization methods as FDM (q-fix), FDM (q-opt), SDM (q-fix), and SDM (q-opt).

The organic molecules considered in this study are depicted in **Figure 3**. The crystal structures of these molecules are retrieved from the CSD, and the H_{subl} data are reported in Ref. [48]. The selection of the eight molecules was based on their molecular weights and diversity of the substituents. They include molecules composed of π-conjugated systems, such as ANTCEN and PENCEN, those with rotatable bonds, such as BIPHEN and TPHBEN, as well as other molecules possessing hydroxyl, carbonyl, and amino groups.

The reference structures of single molecules and PESs were calculated using density functional theory on Gaussian 16 with the basis set 6-311++g(d,p) and the ωB97XD density functional.[72] PESs of dihedral angles were created for all freely rotatable single bonds by evaluating the energies of rotations in 5-degree increments. Methyl groups were excluded from this study as their impact on the quality of FFs is minimal. The initial FF parameters were sourced from GAFF (version 1.8.1[21]). Parameters required for the Ewald method were determined with LAMMPS by setting "kspace style ewald" to 1×10^{-4}. The data generation software Antechamber and Moltemplate were used to generate the initial GAFF parameters, which were calculated with atomic charges from electrostatic potentials using the grid-based method (CHELG).[2,21,73,74] The maximum number of iterations for SLSQP optimization in FDM and SDM was set to 100, with each iteration involving approximately five evaluation function calculations. All methods were implemented in Python 3.8.13 and JAX 0.3.13.[62] The FF parameter optimizations were performed using the SLSQP algorithm from SciPy v1.8.1,[70] and the structure optimizations within the SDM algorithm were executed using JAXOPT0.5.[71] For example, on a computer with an Intel Xeon Gold 6230

2.10 GHz CPU and an NVIDIA GeForce 2080 Ti GPU, the total optimization duration for ACANIL with FDM and SDM was 15 and 23 mins, respectively.

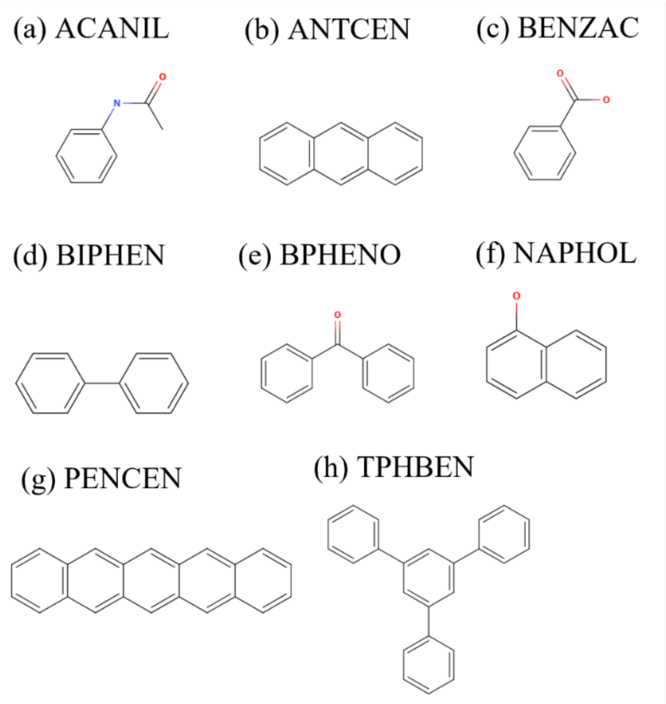
(a) ACANIL
(b) ANTCEN
(c) BENZAC
(d) BIPHEN
(e) BPHENO
(f) NAPHOL
(g) PENCEN
(h) TPHBEN

Figure 3: Eight molecules used for evaluation. The six-letter symbols represent CSD compound IDs. The generic names and complete ID specifying the crystal structure record of the database are shown in parentheses. (a) ACANIL (acetanilide, ACANIL01), (b) ANTCEN (anthracene, ANTCEN), (c) BENZAC (benzoic acid, BENZAC01), (d) BIPHEN (biphenyl, BIPHEN), (e) BPHENO (benzophenone, BIPHENO12), (f) NAPHOL (1-naphthol, NAPHOL01) (g) PENCEN (pentacene, PENCEN), and (h)TPHBEN (1,3,5-triphenyl benzene, TPHBEN01)

3. Results and Discussion

3.1. Optimized Evaluation Functions

Initially, we compared four optimization techniques by evaluating the optimized values of the evaluation functions (Eq. 11). The outcomes of the evaluation function L^{all} after optimization are illustrated in **Figure 4**. The first value for each molecule represents the initial value obtained from GAFF, which serves as the starting point for the following four optimization methods. The second and third values were obtained using FDM, with the second value not involving charge optimization and the atomic charges fixed, while the third value included atomic charge optimization, denoted by "q-fix" and "q-opt" in parentheses, respectively. The fourth and fifth values were obtained using SDM, with the fourth value not involving charge optimization and the fifth value including it.

The reduction ratios from GAFF are tabulated in **Table 2**. These values represent the mean of ten iterations of FF optimization, as the iterative optimization approach of SLSQP accumulates numerical discrepancies, leading to minor variations in the optimized outcomes, as depicted in **Figure S1**. The observed deviations are significantly small and allow the order of the four optimization techniques to be maintained. Upon comparing the reduction rates of the evaluation function derived from GAFF, FDM(q-fix) decreased to 86.0%, while FDM (q-opt) decreased to 77.4%. In contrast, SDM (q-fix) reduced to 31.3%, and SDM (q-opt) decreased to 19.5%. SDM (q-opt) showed approximately a fourfold enhancement in the improvement proportion compared to FDM (q-fix). Comparing SDM (q-fix) and FDM (q-fix), or SDM (q-opt) and FDM (q-opt), we confirmed that SDM outperforms FDM. Moreover, comparing FDM (q-opt) and FDM (q-fix), or SDM (q-opt) and FDM (q-opt), the impact of replacing q-fix with q-opt is also significant.

The significant difference between FDM and SDM can be attributed to the evaluation function used during optimization, specifically L_{FDM}^{all}, which deviates from the function L^{all}. When L_{FDM}^{all} is exactly zero, force $\mathbf{F}$ is zero for the single-molecule and crystal structure $\mathbf{u}'$, making them stable structures. However, it is generally unlikely for L_{FDM}^{all} to be exactly zero because the evaluation function of FDM is overdetermined. In other words, it has fewer variables than independent equations in Eq. (25), as listed in **Table 3**. Consequently, FDM was unable to achieve a solution with L^{all} = 0, resulting in the optimized FFs maintaining non-zero residual forces at the reference structure $\mathbf{u}'$. This prevented the optimized structures $\tilde{\mathbf{u}}$ from matching $\mathbf{u}'$ and the non-zero forces from ensuring that $\tilde{\mathbf{u}}$ is close to $\mathbf{u}'$. Conversely, SDM directly makes $\tilde{\mathbf{u}}$ as close to $\mathbf{u}'$ as possible, by directly seeking the parameter space of $\mathbf{p}$ with the gradient information of L^{all} with respect to the FF parameter $\mathbf{p}$.

The enhancements in q-fix and q-opt methodologies can be attributed to the increase in degrees of freedom, allowing for proper exploration within broader search spaces. The relatively small improvement in PECEN can be attributed to the initially high reproducibility of PECEN's crystal structure by GAFF, as confirmed repeatedly in previous studies on organic semiconductor films using PECEN in MD simulations.[75–77]

In the following sections, we will examine the replicability of crystal structures and lattice energies by comparing the initial GAFF parameters with FDM- and SDM-optimized FFs, incorporating both q-fix and q-opt methodologies. We will analyze the errors corresponding to each term of the evaluation function using the best values of the evaluation functions obtained from the ten FF optimization runs for the four methods. As the evaluation functions of PESs do not include convergence algorithms, which are the subject of this study, the comparative analysis of PES reproducibility is reported in **Figure S3** to **Figure S9**.

Table 2. The reduction ratios of evaluation function values in Eq. (11) from the initial value GAFF after FF parameters optimization with FDM (q-fix), FDM (q-opt), SDM (q-fix), and SDM (q-opt). Each ratio is an average of ten optimization trials for each method. The bottom row shows further averaged values over the eight molecules. Bold values represent the minimum or those within 10% of the minimum values among the four methods.

CSD ID	FDM (q-fix)	FDM (q-opt)	SDM (q-fix)	SDM (q-opt)
ACANIL	0.736	0.920	0.230	**0.097**
ANTCEN	0.237	0.238	**0.199**	**0.197**
BENZAC	0.375	0.334	0.177	**0.110**
BIPHEN	0.489	0.490	**0.057**	**0.061**
BPHENO	2.378	1.645	**0.094**	**0.096**
NAPHOL	1.041	1.041	0.237	**0.140**
PENCEN	1.280	1.186	0.953	**0.717**
TPHBEN	0.341	0.336	0.557	**0.143**
average	0.860	0.774	0.313	**0.195**

Table 3. Comparison of the number of FF parameters and the total dimension of $\boldsymbol{F}^{\mathrm{M}}$ and $\boldsymbol{F}^{\mathrm{C}}$, with the number of equations needed to ensure the evaluation function L_{FDM}^{all} is zero (excluding PES and lattice energy).

CSD ID	Number of FF parameters	Total dimension of $\boldsymbol{F}^{\mathrm{M}}$ and $\boldsymbol{F}^{\mathrm{C}}$
ACANIL	101	519
ANTCEN	33	366
BENZAC	72	411
BIPHEN	53	204
BPHENO	65	366
NAPHOL	81	291
PENCEN	42	546
TPHBEN	62	636

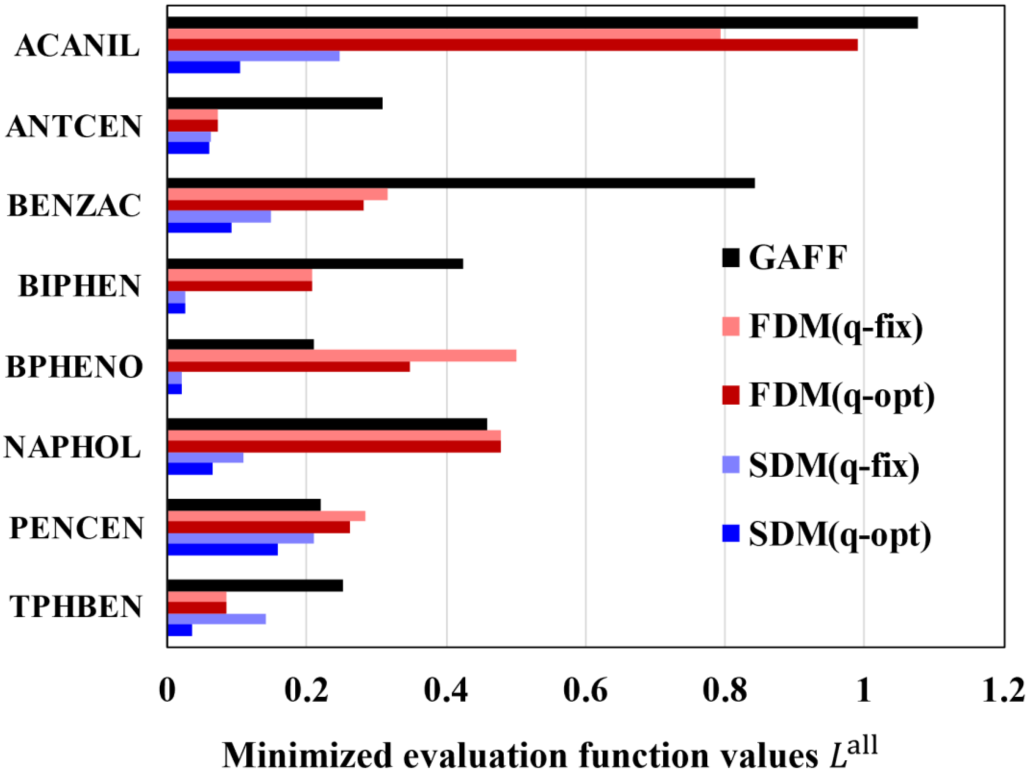

Figure 4. The bar chart displays the evaluation function values for GAFF (initial values) and after optimization using FDM (q-fix), FDM (q-opt), SDM (q-fix), and SDM (q-opt). The values for each method are averaged over ten optimization trials.

3.2. Structure Matching

Figure 5 presents histograms illustrating the errors in lattice constants optimized using initial GAFF and FFs optimized by FDM (q-fix), FDM (q-opt), SDM (q-fix), and SDM (q-opt). **Figure 5(a)** examines the reproducibility of unit cell edge lengths a, b, and c. Comparing the number of edges with errors below 1%, we observe a progression from GAFF to FDM to SDM, with SDM (q-opt) displaying particularly high performance. The reproducibility of SDM(q-opt) is the highest, with 18 out of 24 cases showing errors below 1.0%. Even the worst case of SDM (q-opt) remains within a 4% error margin. **Figure 5(b)** represents the reproducibility of unit cell angles α, β, and γ. The reproducibility of the angles with SDM (q-opt) is also remarkably high, with 22 out of 24 cases showing errors below 0.25%, and the worst case remaining within a 1.25% error margin. In contrast, other methods exhibit errors exceeding 1.25%. Based on these results, we can conclude that the combined use of SDM and q-opt allows for the creation of an FF with the highest reproducibility of lattice constants. **Figure S10** provides further details on the errors for all molecules and their six respective lattice constants.

It is important to note that crystal structures experimentally derived from the CSD using single-crystal X-ray diffraction may differ from the true stable structure, as the experimental measurements are typically conducted at finite temperatures rather than at absolute zero. In this study, we assume that any differences between the experimental and stable structures are negligible. Addressing this discrepancy would require a large amount of crystal structure information at various finite temperatures along with their corresponding energies. However, as mentioned in the introduction, this study focuses on utilizing experimentally obtained crystal structures, and thus, this issue falls outside the scope of this paper as it would require additional

QM calculations for finite-temperature crystal structures and consideration of all these structures as reference structures.

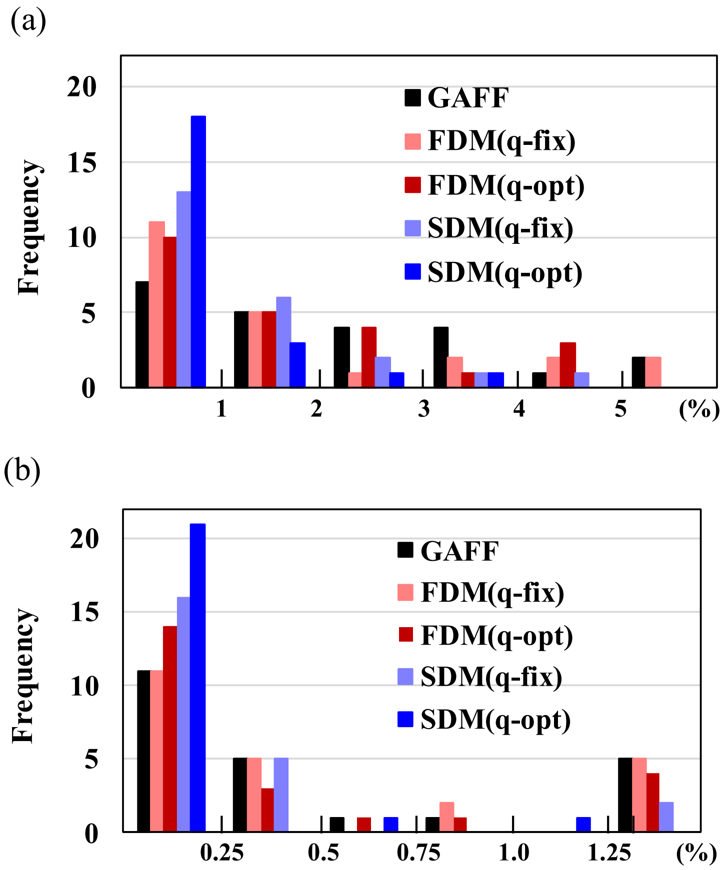

Figure 5. Histograms of optimized lattice constants. (a) Histogram of errors in lengths of axes a, b, and c, optimized with GAFF, FDM, and SDM. The x-axis represents the percentage of errors, with the smallest area corresponding to 0–1% and the largest area representing >5%. (b) Histograms of errors in angles between axes b–c, c–a, and a–b, represented as α, β, and γ respectively, optimized with GAFF, FDM, and SDM. The x-axis represents the percentage of errors, with the smallest area corresponding to 0-0.25% and the largest area representing >1.5%.

To assess the accuracy of molecular orientations and internal lattice structures, we calculated the root mean squared error (RMSE) of internal atomic coordinates in a unit cell, as displayed in **Figure 6**. **Table 4** presents the RMSE values obtained. The average RMSE for all molecules was 0.254 Å with GAFF, 0.244 Å with FDM (q-fix), 0.216 Å with FDM (q-opt), 0.193 Å with SDM (q-fix), and 0.150 Å with SDM. In three out of the eight molecules, both FDM (q-fix) and FDM (q-opt) failed to enhance the accuracy of internal coordinates compared to GAFF. These results suggest that employing both SDM and q-opt enables the development of an FF with the highest reproducibility in terms of internal lattice structures.

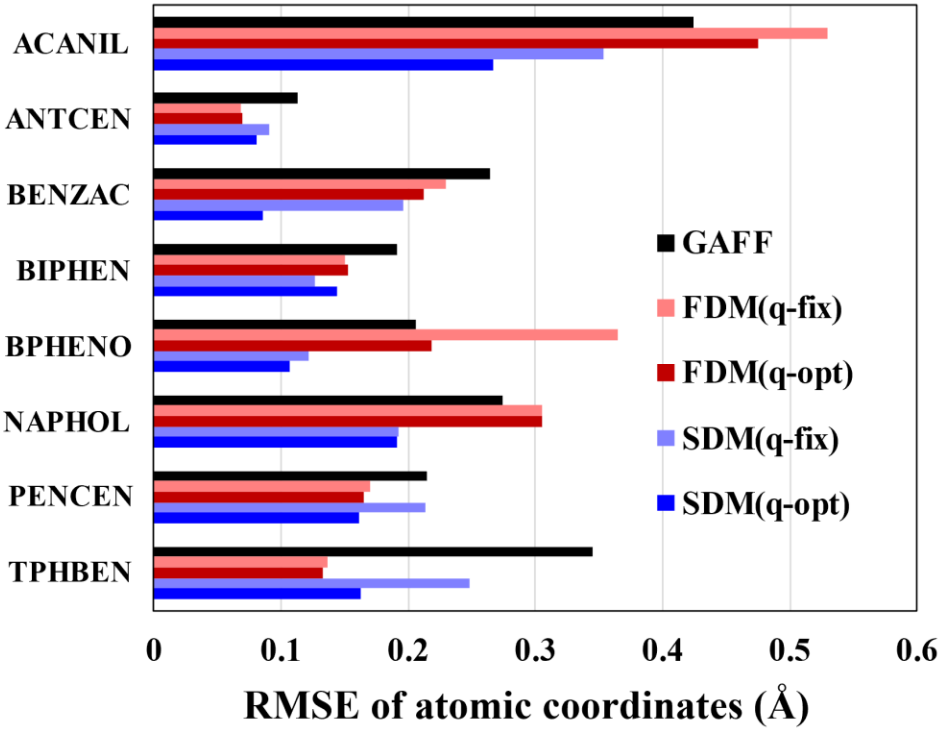

Figure 6. Bar chart of RMSE of internal atomic coordinates obtained using the reference crystal structures.

Table 4. RMSE of internal atomic coordinates in crystal structures (Å).

CSD ID	GAFF	FDM (q-fix)	FDM (q-opt)	SDM (q-fix)	SDM (q-opt)
ACANIL	0.424	0.529	0.475	0.353	**0.267**
ANTCEN	0.113	**0.068**	0.069	0.091	0.080
BENZAC	0.264	0.229	0.213	0.197	**0.086**
BIPHEN	0.192	0.150	0.153	0.127	**0.144**
BPHENO	0.206	0.364	0.218	0.122	**0.106**
NAPHOL	0.274	0.305	0.305	0.193	**0.191**
PENCEN	0.214	0.170	0.165	0.213	**0.161**
TPHBEN	0.344	0.136	**0.132**	0.248	0.162
average	0.254	0.244	0.216	0.193	**0.150**

As shown in **Figure 7**, both FDM (q-fix) and FDM (q-opt) exhibit distorted structures after optimizing the single BENZAC molecules' geometry. The red arrows highlight that the hydrogen atom bonded to an aromatic carbon in the benzene ring deviates from the plane of the ring, and the planar molecule containing the carboxyl group is oriented at an angle. This distortion is attributed to the overdetermined evaluation function, as discussed in section 3.1.

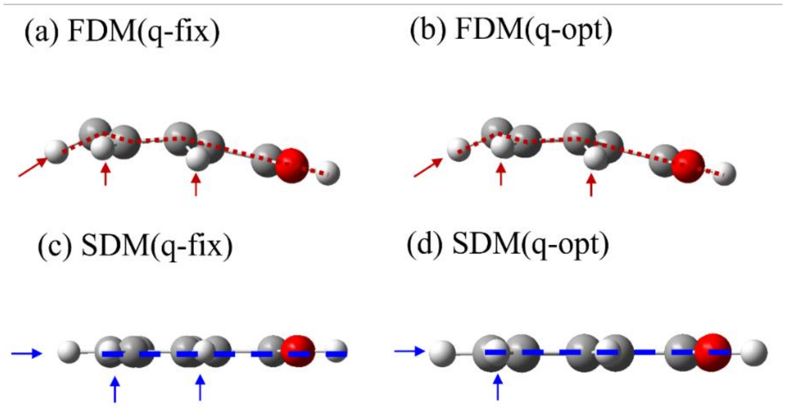

Figure 7. Optimized structures of a single BENZAC molecule by FF derived *via* (a) FDM (q-fix), (b) FDM (q-opt) (c) SDM (q-fix) and (d) SDM (q-opt).

3.3. Lattice Energy Matching

Table 5 presents the lattice energies calculated with GAFF and the FFs optimized using the four methods. Among them, SDM (q-opt) demonstrated the highest accuracy in reproducing the lattice energies. As GAFF is not specifically designed to accurately predict U^{lat} for single molecules, it resulted in large errors. While FDM (q-fix) and FDM (q-opt) showed high accuracy in lattice energy prediction for ANTCEN and TPHBEN, errors for ACANIL, NAPHOL, and BENZAC were significantly larger in the FDM methods compared to the SDM methods. This discrepancy could be attributed to the major intermolecular forces present in the crystal. ANTCEN and TPHBEN are known to be stabilized by π-stacking or vdW forces, whereas ACANIL, NAPHOL, and BENZAC form hydrogen bonds as discussed in detail in section 3.5. Despite BIPHEN and PENCEN not forming hydrogen bonds, it is likely that they could not achieve a balance between maintaining accurate energy matching and other objectives, such as monomer structures, crystal structures, and lattice energy.

In contrast, SDM (q-fix) and SDM (q-opt) methods achieved high accuracy, with errors below 0.3 kcal/mol, except for ANTCEN in SDM (q-fix). ACANIL, NAPHOL, and BENZAC, which form hydrogen bonds, also showed high accuracy with SDM (q-fix) and SDM (q-opt). Although we employed an Amber-type FF, expressed by Eq. (1), which does not explicitly include hydrogen bonds, these results suggest that the intermolecular interactions resulting from vdW and Coulomb forces, along with the indirect correlations between bond, bond angle, and dihedral angle, were able to practically reproduce the hydrogen bonds.

Table 5. Lattice energies and errors (shown in parentheses) obtained from experiments (kcal/mol) using the FFs optimized with GAFF (initial values), FDM (q-fix), FDM (q-opt), SDM (q-fix), and SDM (q-opt). The bottom line 'RMSE' expresses the root mean squared error over eight molecules.

CSD ID	Ref.	GAFF		FDM (q-fix)		FDM (q-opt)		SDM (q-fix)		SDM (q-opt)	
ACANIL	-25.04	-19.95	(5.09)	-30.06	(-5.02)	-31.65	(-6.61)	-25.31	(-0.27)	**-24.87**	**(0.17)**
ANTCEN	-25.13	-20.46	(4.68)	**-25.07**	**(0.07)**	**-25.08**	**(0.05)**	-24.19	(0.94)	**-25.06**	**(0.07)**
BENZAC	-22.50	-16.27	(6.23)	-19.59	(2.91)	-24.38	(-1.88)	-22.41	(0.09)	**-22.46**	**(0.05)**
BIPHEN	-21.07	-17.56	(3.51)	-20.27	(0.80)	-20.31	(0.77)	-20.92	(0.15)	**-20.97**	**(0.11)**
BPHENO	-22.48	-19.44	(3.04)	-21.99	(0.49)	-20.53	(1.95)	-22.52	(-0.04)	**-22.46**	**(0.02)**
NAPHOL	-22.98	-18.41	(4.57)	-18.42	(4.56)	-18.42	(4.56)	**-22.88**	**(0.10)**	**-22.88**	**(0.10)**
PENCEN	-30.11	-33.52	(-3.41)	-32.03	(-1.91)	-30.70	(-0.59)	**-30.06**	**(0.05)**	-30.35	(-0.23)
TPHBEN	-36.51	-33.33	(3.18)	**-36.51**	**(0.00)**	**-36.51**	**(0.00)**	-36.46	(0.05)	**-36.53**	**(-0.02)**
RMSE			(4.34)		(2.72)		(3.04)		(0.36)		**(0.12)**

3.4.Crystal Structure Reproducibility on Supercells and at Finite Temperature

MD simulations were performed on supercells containing more than 3000 molecules using a time step of 1 fs to ensure the preservation of all crystal structures. The FFs optimized with SDM (q-opt) were used for the simulations, which were conducted under NPT conditions at 300 K. The simulation process involved heating from 10 K to 300 K over 0.1 ns, maintaining at 300 K for 1 ns, and then cooling back to 10 K over 0.1 ns. The lattice constants of the eight crystal molecules after the MD simulations with supercells are summarized in **Table 6**, where the axis lengths were converted to those in unit cells. Despite the weak hydrogen bonding between the amino and carbonyl groups of ACANIL, the crystal structure was successfully reproduced, as shown in **Figure 8**. Additionally, the structures obtained from the MD simulations under the same conditions for the other seven molecules are presented in **Figure S11** to **Figure S17**.

Table 6. Lattice constants of the supercell models obtained after MD simulations at 300 K and NPT conditions, with errors (in parentheses), compared to experimental crystal structures (kcal/mol). The lengths were divided by the multiples to facilitate effective comparison between the supercells and the lattice constants of the unit cells.

CSD ID	a (Å)		b (Å)		c (Å)		α(degree)		β(degree)		γ(degree)	
ACANIL	19.48	(-0.03)	9.23	(-0.13)	8.00	(0.22)	89.82	(-0.19)	90.01	(0.01)	90.01	(0.01)
ANTCEN	17.11	(-0.02)	6.10	(0.07)	11.23	(0.05)	90.25	(0.25)	123.95	(-0.75)	89.85	(-0.15)
BENZAC	10.96	(-0.06)	5.27	(0.11)	22.04	(0.06)	90.10	(0.10)	98.30	(0.89)	90.16	(0.16)
BIPHEN	8.18	(0.06)	5.62	(-0.02)	9.46	(-0.01)	89.88	(-0.12)	95.04	(-0.36)	90.03	(0.03)
BPHENO	7.79	(0.05)	10.21	(-0.03)	12.03	(-0.01)	90.19	(0.19)	89.71	(-0.29)	89.99	(-0.01)
NAPHOL	13.24	(0.06)	4.77	(-0.03)	13.25	(-0.03)	90.06	(0.06)	117.35	(0.23)	89.89	(-0.11)
PENCEN	15.78	(-0.02)	6.05	(-0.01)	16.00	(-0.01)	100.57	(-1.33)	111.91	(-0.69)	85.95	(0.15)
TPHBEN	7.89	(0.28)	18.15	(-1.61)	10.66	(-0.59)	90.03	(0.03)	90.00	(0.00)	89.44	(-0.56)

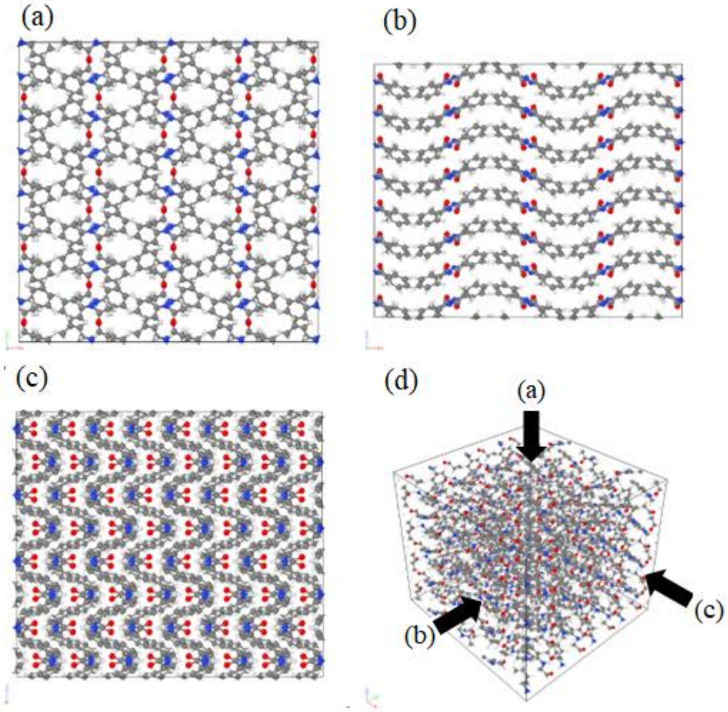

Figure 8. A supercell structure of ACANIL Crystal Structure after 1 ns of 300 K MD using the FFs optimized with SDM (q-opt).

3.5. Charge Optimization with Differentiable Ewald Method

We start by discussing the differences between q-fix and q-opt. **Figure 9** displays the changes in atomic charges for each atom in SDM (q-fix) and SDM (q-opt). As explained in the Methodology section, SDM (q-fix) employs charge values calculated from single-molecule first-principles calculations, while SDM (q-opt) optimizes the FFs using the charges from SDM (q-fix) as initial values, based on the evaluation function shown in Eq. (11). The changes in charges are depicted using colors, with molecules composed of π-conjugated systems, such as ANTCEN, BIPHEN, PENCEN, and TPHBEN, showing small charge changes. However, ACANIL, BENZAC, NAPHOL, and BPHENO exhibit more significant changes in charges. However, changes in the charge for BPHENO are less pronounced than those in the other three.

In **Figure 9(a)**, for instance, ACANIL, the hydrogen bond donor (H of the NH in the amide bond) releases electrons, resulting in a positive shift in charge, while the hydrogen bond acceptor (O of the carbonyl group) accepts electrons, leading to a negative shift in charge. This suggests that the hydrogen bonds were effectively incorporated by considering crystal structures. **Figure 10(a)** further illustrates a section of the ACANIL crystal structure based on the FFs optimized with SDM (q-opt), showing how ACANIL molecules connect in a bead-like chain through hydrogen bonds between the carbonyl oxygen (O) of the amide bond and the hydrogen (H) of the NH group. The expansion of this hydrogen bond network results in relatively large charge changes. Additionally, the charge changes in ACANIL, where the methyl group becomes more positive and the benzene ring more negative, may be attributed to charge compensation due to charge transfer to the amide bond and the need to accurately reproduce PESs of the dihedral angles.

In **Figure 9(c)** for BENZAC, the hydrogen bond donor (H of the OH in the carbonyl group) and the hydrogen bond acceptor (O of the carbonyl group) exchange electrons based on their respective roles in hydrogen bonding. In the crystal, every two molecules form a dimer with double hydrogen bonds, as depicted in **Figure 10(b)**. The charge change in the ortho-position H is believed to enhance the reproduction of the dihedral angle PES.

Similarly, in **Figure 9(f)** for NAPHOL, the H of the OH group acts as a hydrogen bond donor and releases electrons. As illustrated in **Figure 10(c)**, NAPHOL also forms hydrogen bond chains in the crystal, which promotes charge changes. Additionally, the neighboring H atoms are presumed to have changed to improve the accuracy of reproducing the dihedral angle PES.

As evident from **Figure 9** and **Figure 10,** significant charge changes occur in regions that form hydrogen bonds within crystals after optimization. The FF optimization in this study considers both monomer and crystal structures, with initial charges calculated in the monomer. Thus, charges are shifted during optimization to accommodate both aspects while preserving the crystal structure. However, it is worth noting that a limitation of non-polarizable FF optimization is its inability to accurately capture dynamic changes in actual charges between different states. The incorporation of SDM into polarizable FFs could potentially address these limitations.

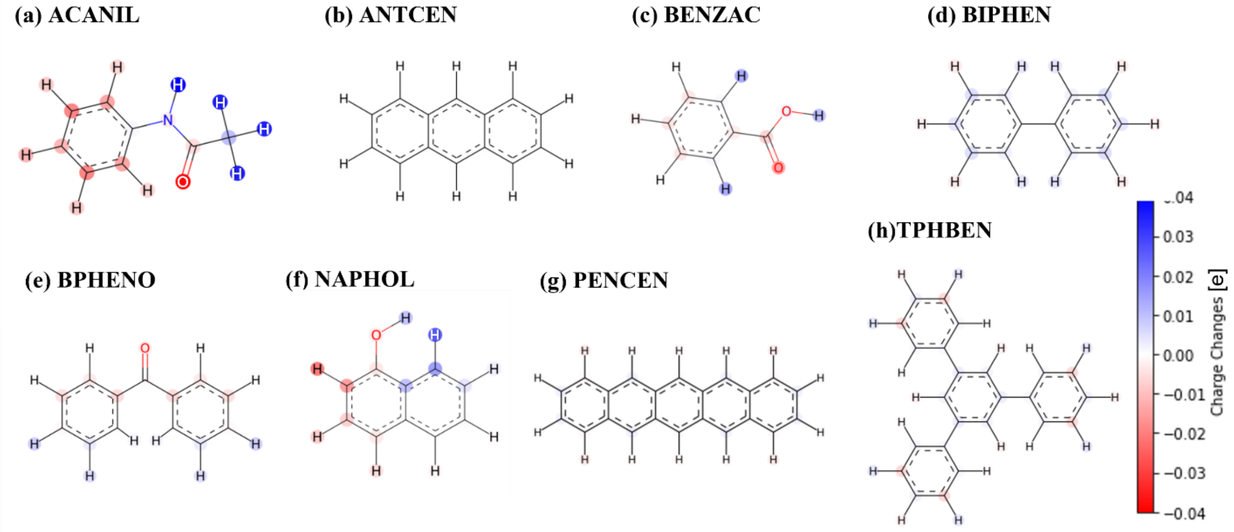

Figure 9. Charge changes for all eight molecules used as motifs after FF optimization using SDM (q-opt). Blue color represents atoms that shifted positively (gained charge) after optimization, while red color indicates atoms that shifted negatively (lost charge).

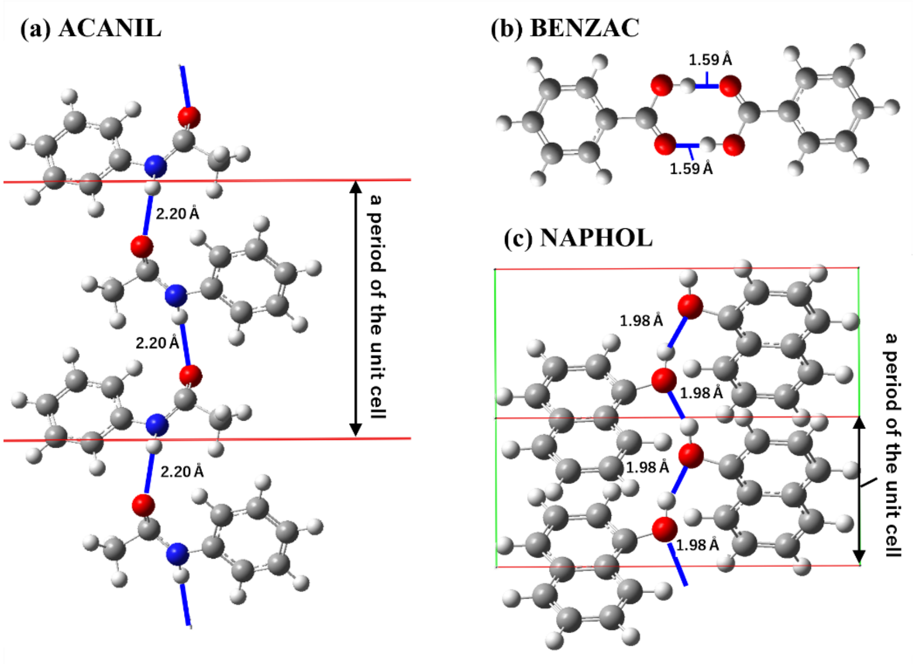

Figure 10. Hydrogen bonds in (a) ACANIL, (b) BENZAC, and (c) NAPHOL of the optimized crystal structures with the FF generated by SDM (q-opt).

4. Conclusion

We proposed the SDM as a novel approach for generating FFs of small organic molecules using multiple types of reference data, including (i) stable monomer structures, (ii) crystal structures, (iii) lattice energy of the crystal structure, and (iv) PESs of the dihedral angles. SDM incorporates an IFD scheme to differentiate the converged structures of iterative algorithms with respect to the FF parameters, allowing for reproducibility of experimental crystal structures. Furthermore, to accurately account for long-range interactions when optimizing atomic charges, we implemented the Ewald method in its differentiable form.

Comparing the optimization results of FFs using FDM (q-fix), FDM (q-opt), SDM (q-fix), and SDM (q-opt) with evaluation functions representing the magnitude of errors, we observed respective error factors of 0.860, 0.774, 0.313, and 0.195, respectively. Switching from FDM to SDM resulted in a significant improvement, and further combining it with q-opt showed that SDM (q-opt) can reduce the error to less than 1/4 of FDM (q-fix).

Consistently, the lattice constants, atomic arrangements within the crystal, and lattice energies exhibited higher reproducibility in SDM compared to FDM and q-opt to q-fix. The SDM (q-opt) method achieved accurate results for all eight molecules, with lattice constant errors less than 4% for edge lengths and less than 1.25% for angles. The errors in internal atomic coordinates averaged 0.15 Å, and the lattice energy errors were 0.12 kcal/mol. Additionally, we performed MD simulations at 300 K under NPT conditions and confirmed the preservation of all crystal structures.

The favorable characteristics of the SDM method stem from its unique ability to directly differentiate the errors between the calculated crystal structures obtained through the convergence algorithm and the experimentally obtained crystal structures (excluding errors due to finite temperature), with respect to each FF parameter. This allows for precise adjustment of FF parameters, including charges, to ensure accurate reproduction of hydrogen bonding interactions, especially for molecules forming hydrogen bonds within the crystal. The q-opt method, which employs a differentiable Ewald method for charge optimization, enables the creation of FFs that can effectively capture the subtle nuances of hydrogen bonding in crystal structures.

Importantly, the versatility of SDM extends beyond Amber-type FFs, and it can be readily applied to polarized FFs and special interactions explicitly described as an energy function, such as hydrogen bonding. This makes SDM a promising method for parameterizing FFs with crystal structures, and we believe that it will emerge as a new standard in the field.

Associated Content

Supporting Information

The supporting information includes energy comparisons between our program and LAMMPS, detailed parameters of the optimization algorithms, boxplots of the optimized evaluation functions from ten trials using four different methods, PES plots for all dihedral angles, and crystal structures resulting from MD simulations of supercells under NPT conditions.

Code Availability

The code and data are available at github.com/n-hiroshi/delff.

Author Information

Corresponding Author

Hiroshi Nakano - Material and Device Analysis Center, Sony Semiconductor Solutions Corporation 4-14-1, Asahi-cho, Atsugi, Kanagawa, Japan; orcid.org/0000-0003-2745-9340; E-mail: Hiroshi.B.Nakano@sony.com

Authors

Shinnosuke Hattori - Material and Device Analysis Center, Sony Semiconductor Solutions Corporation 4-14-1, Asahi-cho, Atsugi, Kanagawa, Japan

Hajime Kobayashi - Material and Device Analysis Center, Sony Semiconductor Solutions Corporation 4-14-1, Asahi-cho, Atsugi, Kanagawa, Japan; orcid.org/0000-0002-4759-3937

Takumi Araki - Material and Device Analysis Center, Sony Semiconductor Solutions Corporation 4-14-1, Asahi-cho, Atsugi, Kanagawa, Japan

Masakazu Ukita - Material and Device Analysis Center, Sony Semiconductor Solutions Corporation 4-14-1, Asahi-cho, Atsugi, Kanagawa, Japan

Toshio Nishi - Material and Device Analysis Center, Sony Semiconductor Solutions Corporation 4-14-1, Asahi-cho, Atsugi, Kanagawa, Japan

Yoshihiro Kudo - Material and Device Analysis Center, Sony Semiconductor Solutions Corporation 4-14-1, Asahi-cho, Atsugi, Kanagawa, Japan

Notes

The authors declare no competing financial interest.

References

(1) Case, D. A.; Metin Aktulga, H.; Belfon, K.; Ben-Shalom, I.; Brozell, S. R.; Cerutti, D. S.; Cheatham, T. E., III; Cruzeiro, V. W. D.; Darden, T. A.; Duke, R. E.; Giambasu, G.; Gilson, M. K.; Gohlke, H.; Goetz, A. W.; Harris, R.; Izadi, S.; Izmailov, S. A.; Jin, C.; Kasavajhala, K.; Kaymak, M. C.; King, E.; Kovalenko, A.; Kurtzman, T.; Lee, T.; LeGrand, S.; Li, P.; Lin, C.; Liu, J.; Luchko, T.; Luo, R.; Machado, M.; Man, V.; Manathunga, M.; Merz, K. M.; Miao, Y.; Mikhailovskii, O.; Monard, G.; Nguyen, H.; O'Hearn, K. A.; Onufriev, A.; Pan, F.; Pantano, S.; Qi, R.; Rahnamoun, A.; Roe, D. R.; Roitberg, A.; Sagui, C.; Schott-Verdugo, S.; Shen, J.; Simmerling, C. L.; Skrynnikov, N. R.; Smith, J.; Swails, J.; Walker, R. C.; Wang, J.; Wei, H.; Wolf, R. M.; Wu, X.; Xue, Y.; York, D. M.; Zhao, S.; Kollman, P. A. *Amber 2021*; University of California, San Francisco, 2021.

(2) Thompson, A. P.; Aktulga, H. M.; Berger, R.; Bolintineanu, D. S.; Brown, W. M.; Crozier, P. S.; in 't Veld, P. J.; Kohlmeyer, A.; Moore, S. G.; Nguyen, T. D.; Shan, R.; Stevens, M. J.; Tranchida, J.; Trott, C.; Plimpton, S. J. LAMMPS - a Flexible Simulation Tool for Particle-Based Materials Modeling at the Atomic, Meso, and Continuum Scales. *Comput. Phys. Commun.* **2022**, *271*, 108171.

(3) Vanommeslaeghe, K.; Hatcher, E.; Acharya, C.; Kundu, S.; Zhong, S.; Shim, J.; Darian, E.; Guvench, O.; Lopes, P.; Vorobyov, I.; Mackerell, A. D., Jr. CHARMM General Force Field: A Force Field for Drug-like Molecules Compatible with the CHARMM All-Atom Additive Biological Force Fields. *J. Comput. Chem.* **2010**, *31* (4), 671–690.

(4) Yang, Y.; Qin, J.; Liu, H.; Yao, X. Molecular Dynamics Simulation, Free Energy Calculation and Structure-Based 3D-QSAR Studies of B-RAF Kinase Inhibitors. *J. Chem. Inf. Model.* **2011**, *51* (3), 680–692.

(5) Wang, X.; Song, K.; Li, L.; Chen, L. Structure-Based Drug Design Strategies and Challenges. *Curr. Top. Med. Chem.* **2018**, *18* (12), 998–1006.

(6) Opo, F. A. D. M.; Rahman, M. M.; Ahammad, F.; Ahmed, I.; Bhuiyan, M. A.; Asiri, A. M. Structure Based Pharmacophore Modeling, Virtual Screening, Molecular Docking and ADMET Approaches for Identification of Natural Anti-Cancer Agents Targeting XIAP Protein. *Sci. Rep.* **2021**, *11* (1), 4049.

(7) Ganguly, A.; Tsai, H.-C.; Fernández-Pendás, M.; Lee, T.-S.; Giese, T. J.; York, D. M. AMBER Drug Discovery Boost Tools: Automated Workflow for Production Free-Energy Simulation Setup and Analysis (ProFESSA). *J. Chem. Inf. Model.* **2022**, *62* (23), 6069–6083.

(8) Kippelen, B.; Brédas, J.-L. Organic Photovoltaics. *Energy Environ. Sci.* **2009**, *2* (3), 251–261.

(9) Kobayashi, H.; Kobayashi, N.; Hosoi, S.; Koshitani, N.; Murakami, D.; Shirasawa, R.; Kudo, Y.; Hobara, D.; Tokita, Y.; Itabashi, M. Hopping and Band Mobilities of Pentacene, Rubrene, and 2,7-Dioctyl[1]Benzothieno[3,2-b][1]Benzothiophene (C8-BTBT) from First Principle Calculations. *J. Chem. Phys.* **2013**, *139* (1), 014707.

(10) Friederich, P.; Fediai, A.; Kaiser, S.; Konrad, M.; Jung, N.; Wenzel, W. Toward Design of Novel Materials for Organic Electronics. *Adv. Mater.* **2019**, *31* (26), e1808256.

(11) Honig, B.; Karplus, M. Implications of Torsional Potential of Retinal Isomers for Visual Excitation. *Nature* **1971**, *229* (5286), 558–560.

(12) Warshel, A.; Karplus, M. Calculation of Ground and Excited State Potential Surfaces of Conjugated Molecules. I. Formulation and Parametrization. *J. Am. Chem. Soc.* **1972**, *94* (16), 5612–5625.

(13) Warshel, A.; Karplus, M. Calculation of Pi-Pi Excited State Conformations and Vibronic Structure of Retinal and Related Molecules. *J. Am. Chem. Soc.* **1974**, *96* (18), 5677–5689.

(14) Karplus, M. Development of Multiscale Models for Complex Chemical Systems: From H+H_2 to Biomolecules (Nobel Lecture). *Angew. Chem. Int. Ed Engl.* **2014**, *53* (38), 9992–10005.

(15) Levitt, M. Birth and Future of Multiscale Modeling for Macromolecular Systems (Nobel Lecture). *Angew. Chem. Int. Ed Engl.* **2014**, *53* (38), 10006–10018.

(16) Warshel, A. Multiscale Modeling of Biological Functions: From Enzymes to Molecular Machines (Nobel Lecture). *Angew. Chem. Int. Ed Engl.* **2014**, *53* (38), 10020–10031.

(17) Chung, L. W.; Sameera, W. M. C.; Ramozzi, R.; Page, A. J.; Hatanaka, M.; Petrova, G. P.; Harris, T. V.; Li, X.; Ke, Z.; Liu, F.; Li, H.-B.; Ding, L.; Morokuma, K. The ONIOM Method and Its Applications. *Chem. Rev.* **2015**, *115* (12), 5678–5796.

(18) Zev, S.; Gupta, P. K.; Pahima, E.; Major, D. T. A Benchmark Study of Quantum Mechanics and Quantum Mechanics-Molecular Mechanics Methods for Carbocation Chemistry. *J. Chem. Theory Comput.* **2022**, *18* (1), 167–178.

(19) Dong, G.; Phung, Q. M.; Pierloot, K.; Ryde, U. Reaction Mechanism of [NiFe] Hydrogenase Studied by Computational Methods. *Inorg. Chem.* **2018**, *57* (24), 15289–15298.

(20) Mayo, S. L.; Olafson, B. D.; Goddard, W. A. DREIDING: A Generic Force Field for Molecular Simulations. *J. Phys. Chem.* **1990**, *94* (26), 8897–8909.

(21) Wang, J.; Wolf, R. M.; Caldwell, J. W.; Kollman, P. A.; Case, D. A. Development and Testing of a General Amber Force Field. *J. Comput. Chem.* **2004**, *25* (9), 1157–1174.

(22) Qiu, Y.; Smith, D. G. A.; Boothroyd, S.; Jang, H.; Hahn, D. F.; Wagner, J.; Bannan, C. C.; Gokey, T.; Lim, V. T.; Stern, C. D.; Rizzi, A.; Tjanaka, B.; Tresadern, G.; Lucas, X.; Shirts, M. R.; Gilson, M. K.; Chodera, J. D.; Bayly, C. I.; Mobley, D. L.; Wang, L.-P. Development and Benchmarking of Open Force Field v1.0.0-the Parsley Small-Molecule Force Field. *J. Chem. Theory Comput.* **2021**, *17* (10), 6262–6280.

(23) Behler, J.; Parrinello, M. Generalized Neural-Network Representation of High-Dimensional Potential-Energy Surfaces. *Phys. Rev. Lett.* **2007**, *98* (14), 146401.

(24) Ko, T. W.; Finkler, J. A.; Goedecker, S.; Behler, J. A Fourth-Generation High-Dimensional Neural Network Potential with Accurate Electrostatics Including Non-Local Charge Transfer. *Nat. Commun.* **2021**, *12* (1), 398.

(25) Herbold, M.; Behler, J. A Hessian-Based Assessment of Atomic Forces for Training Machine Learning Interatomic Potentials. *J. Chem. Phys.* **2022**, *156* (11), 114106.

(26) Smith, J. S.; Isayev, O.; Roitberg, A. E. ANI-1: An Extensible Neural Network Potential with DFT Accuracy at Force Field Computational Cost. *Chem. Sci.* **2017**, *8* (4), 3192–3203.

(27) Smith, J. S.; Nebgen, B. T.; Zubatyuk, R.; Lubbers, N.; Devereux, C.; Barros, K.; Tretiak, S.; Isayev, O.; Roitberg, A. E. Approaching Coupled Cluster Accuracy with a General-Purpose Neural Network Potential through Transfer Learning. *Nat. Commun.* **2019**, *10* (1), 2903.

(28) Gao, X.; Ramezanghorbani, F.; Isayev, O.; Smith, J. S.; Roitberg, A. E. TorchANI: A Free and Open Source PyTorch-Based Deep Learning Implementation of the ANI Neural Network Potentials. *J. Chem. Inf. Model.* **2020**, *60* (7), 3408–3415.

(29) Devereux, C.; Smith, J. S.; Huddleston, K. K.; Barros, K.; Zubatyuk, R.; Isayev, O.; Roitberg, A. E. Extending the Applicability of the ANI Deep Learning Molecular Potential to Sulfur and Halogens. *J. Chem. Theory Comput.* **2020**, *16* (7), 4192–4202.

(30) Hao, D.; He, X.; Roitberg, A. E.; Zhang, S.; Wang, J. Development and Evaluation of Geometry Optimization Algorithms in Conjunction with ANI Potentials. *J. Chem. Theory Comput.* **2022**, *18* (2), 978–991.

(31) Schütt, K. T.; Sauceda, H. E.; Kindermans, P.-J.; Tkatchenko, A.; Müller, K.-R. SchNet - A Deep Learning Architecture for Molecules and Materials. *J. Chem. Phys.* **2018**, *148* (24), 241722.

(32) Gasteiger, J.; Groß, J.; Günnemann, S. Directional Message Passing for Molecular Graphs, 2023. https://openreview.net/pdf?id=B1eWbxStPH (accessed 2023-04-02).

(33) Gasteiger, J.; Giri, S.; Margraf, J. T.; Günnemann, S. Fast and Uncertainty-Aware Directional Message Passing for Non-Equilibrium Molecules. *arXiv [cs.LG]*, 2020. http://arxiv.org/abs/2011.14115.

(34) Takamoto, S.; Shinagawa, C.; Motoki, D.; Nakago, K.; Li, W.; Kurata, I.; Watanabe, T.; Yayama, Y.; Iriguchi, H.; Asano, Y.; Onodera, T.; Ishii, T.; Kudo, T.; Ono, H.; Sawada, R.; Ishitani, R.; Ong, M.; Yamaguchi, T.; Kataoka, T.; Hayashi, A.; Charoenphakdee, N.; Ibuka, T. Towards Universal Neural Network Potential for Material Discovery Applicable to Arbitrary Combination of 45 Elements. *Nat. Commun.* **2022**, *13* (1), 2991.

(35) Takamoto, S.; Izumi, S.; Li, J. TeaNet: Universal Neural Network Interatomic Potential Inspired by Iterative Electronic Relaxations. *Comput. Mater. Sci.* **2022**, *207*, 111280.

(36) Thaler, S.; Zavadlav, J. Learning Neural Network Potentials from Experimental Data via Differentiable Trajectory Reweighting. *Nat. Commun.* **2021**, *12* (1), 6884.

(37) Drautz, R. Atomic Cluster Expansion for Accurate and Transferable Interatomic Potentials. *Phys. Rev. B Condens. Matter* **2019**, *99* (1), 014104.

(38) Lysogorskiy, Y.; Oord, C. van der; Bochkarev, A.; Menon, S.; Rinaldi, M.; Hammerschmidt, T.; Mrovec, M.; Thompson, A.; Csányi, G.; Ortner, C.; Drautz, R. Performant Implementation of the Atomic Cluster Expansion (PACE) and Application to Copper and Silicon. *NPJ Comput. Mater.* **2021**, *7* (1), 1–12.

(39) Bochkarev, A.; Lysogorskiy, Y.; Menon, S.; Qamar, M.; Mrovec, M.; Drautz, R. Efficient Parametrization of the Atomic Cluster Expansion. *Phys. Rev. Materials* **2022**, *6* (1), 013804.

(40) Boothroyd, S.; Madin, O. C.; Mobley, D. L.; Wang, L.-P.; Chodera, J. D.; Shirts, M. R. Improving Force Field Accuracy by Training against Condensed-Phase Mixture Properties. *J. Chem. Theory Comput.* **2022**, *18* (6), 3577–3592.

(41) Boothroyd, S.; Wang, L.-P.; Mobley, D. L.; Chodera, J. D.; Shirts, M. R. Open Force Field Evaluator: An Automated, Efficient, and Scalable Framework for the Estimation of Physical Properties from Molecular Simulation. *J. Chem. Theory Comput.* **2022**, *18* (6), 3566–3576.

(42) Ozpinar, G. A.; Peukert, W.; Clark, T. An Improved Generalized AMBER Force Field (GAFF) for Urea. *J. Mol. Model.* **2010**, *16* (9), 1427–1440.

(43) Park, H.; Zhou, G.; Baek, M.; Baker, D.; DiMaio, F. Force Field Optimization Guided by Small Molecule Crystal Lattice Data Enables Consistent Sub-Angstrom Protein-Ligand Docking. *J. Chem. Theory Comput.* **2021**, *17* (3), 2000–2010.

(44) Thürlemann, M.; Böselt, L.; Riniker, S. Regularized by Physics: Graph Neural Network Parametrized Potentials for the Description of Intermolecular Interactions. *J. Chem. Theory Comput.* **2023**. https://doi.org/10.1021/acs.jctc.2c00661.

(45) Shalev, O.; Shtein, M. Effect of Crystal Density on Sublimation Properties of Molecular Organic Semiconductors. *Org. Electron.* **2013**, *14* (1), 94–99.

(46) Marchese Robinson, R. L.; Geatches, D.; Morris, C.; Mackenzie, R.; Maloney, A. G. P.; Roberts, K. J.; Moldovan, A.; Chow, E.; Pencheva, K.; Vatvani, D. R. M. Evaluation of Force-Field Calculations of Lattice Energies on a Large Public Dataset, Assessment of Pharmaceutical Relevance, and Comparison to Density Functional Theory. *J. Chem. Inf. Model.* **2019**, *59* (11), 4778–4792.

(47) Chickos, J. S.; Gavezzotti, A. Sublimation Enthalpies of Organic Compounds: A Very Large Database with a Match to Crystal Structure Determinations and a Comparison with Lattice Energies. *Cryst. Growth Des.* **2019**, *19* (11), 6566–6576.

(48) McDonagh, J. L.; Palmer, D. S.; van Mourik, T.; Mitchell, J. B. O. Are the Sublimation Thermodynamics of Organic Molecules Predictable? *J. Chem. Inf. Model.* **2016**, *56* (11), 2162–2179.

(49) Xie, Y.; Vandermause, J.; Sun, L.; Cepellotti, A.; Kozinsky, B. Bayesian Force Fields from Active Learning for Simulation of Inter-Dimensional Transformation of Stanene. *NPJ Comput. Mater.* **2021**, *7* (1), 1–10.

(50) Vandermause, J.; Torrisi, S. B.; Batzner, S.; Xie, Y.; Sun, L.; Kolpak, A. M.; Kozinsky, B. On-the-Fly Active Learning of Interpretable Bayesian Force Fields for Atomistic Rare Events. *NPJ Comput. Mater.* **2020**, *6* (1), 1–11.

(51) Köfinger, J.; Hummer, G. Empirical Optimization of Molecular Simulation Force Fields by Bayesian Inference. *Eur. Phys. J. B* **2021**, *94* (12), 245.

(52) Liu, H.; Fu, Z.; Li, Y.; Sabri, N. F. A.; Bauchy, M. Parameterization of Empirical Forcefields for Glassy Silica Using Machine Learning. *MRS Commun.* **2019**, *9* (2), 593–599.

(53) Befort, B. J.; DeFever, R. S.; Maginn, E. J.; Dowling, A. W. Machine Learning-Enabled Optimization of Force Fields for Hydrofluorocarbons. *Comput. Aid. Chem. Eng.* 2022, 49, 1249–1254. https://doi.org/10.1016/b978-0-323-85159-6.50208-6.

(54) Krishnamoorthy, A.; Mishra, A.; Kamal, D.; Hong, S.; Nomura, K.-I.; Tiwari, S.; Nakano, A.; Kalia, R.; Ramprasad, R.; Vashishta, P. EZFF: Python Library for Multi-Objective Parameterization and Uncertainty Quantification of Interatomic Forcefields for Molecular Dynamics. *SoftwareX* **2021**, *13* (100663), 100663.

(55) Furman, D.; Carmeli, B.; Zeiri, Y.; Kosloff, R. Enhanced Particle Swarm Optimization Algorithm: Efficient Training of ReaxFF Reactive Force Fields. *J. Chem. Theory Comput.* **2018**, *14* (6), 3100–3112.

(56) Lombardo, T.; Hoock, J.-B.; Primo, E. N.; Ngandjong, A. C.; Duquesnoy, M.; Franco, A. A. Accelerated Optimization Methods for Force-field Parametrization in Battery Electrode Manufacturing Modeling. *Batter. Supercaps* **2020**, *3* (8), 721–730.

(57) Wang, L.-P.; Chen, J.; Van Voorhis, T. Systematic Parametrization of Polarizable Force Fields from Quantum Chemistry Data. *J. Chem. Theory Comput.* **2013**, *9* (1), 452–460.

(58) Wang, L.-P.; Martinez, T. J.; Pande, V. S. Building Force Fields: An Automatic, Systematic, and Reproducible Approach. *J. Phys. Chem. Lett.* **2014**, *5* (11), 1885–1891.

(59) Qiu, Y.; Nerenberg, P. S.; Head-Gordon, T.; Wang, L.-P. Systematic Optimization of Water Models Using Liquid/Vapor Surface Tension Data. *J. Phys. Chem. B* **2019**, *123* (32), 7061–7073.

(60) Morado, J.; Mortenson, P. N.; Verdonk, M. L.; Ward, R. A.; Essex, J. W.; Skylaris, C.-K. ParaMol: A Package for Automatic Parameterization of Molecular Mechanics Force Fields. *J. Chem. Inf. Model.* **2021**, *61* (4), 2026–2047.

(61) Baydin, A. G.; Pearlmutter, B. A.; Radul, A. A.; Siskind, J. M. Automatic Differentiation in Machine Learning: A Survey. *J. Mach. Leanr. Res.* **2018**, *18*, 1–43.

(62) *Jax: Composable Transformations of Python+NumPy Programs: Differentiate, Vectorize, JIT to GPU/TPU, and More*; Github.

(63) Schoenholz, S. S.; Cubuk, E. D. JAX, M.D.: A Framework for Differentiable Physics. *arXiv [physics.comp-ph]*, 2019. http://arxiv.org/abs/1912.04232.

(64) Goodrich, C. P.; King, E. M.; Schoenholz, S. S.; Cubuk, E. D.; Brenner, M. P. Designing Self-Assembling Kinetics with Differentiable Statistical Physics Models. *Proc. Natl. Acad. Sci. U. S. A.* **2021**, *118* (10). https://doi.org/10.1073/pnas.2024083118.

(65) Kaymak, M. C.; Rahnamoun, A.; O’Hearn, K. A.; van Duin, A. C. T.; Merz, K. M., Jr; Aktulga, H. M. JAX-ReaxFF: A Gradient-Based Framework for Fast Optimization of Reactive Force Fields. *J. Chem. Theory Comput.* **2022**, *18* (9), 5181–5194.

(66) Blondel, M.; Berthet, Q.; Cuturi, M.; Frostig, R.; Hoyer, S.; Llinares-López, F.; Pedregosa, F.; Vert, J.-P. Efficient and Modular Implicit Differentiation. *arXiv [cs.LG]*, 2021. http://arxiv.org/abs/2105.15183.

(67) Ewald, P. P. Ewald Summation. *Ann. Phys.* **1921**, *369* (253), 1–2.

(68) Darden, T.; York, D.; Pedersen, L. Particle Mesh Ewald: An N·log(N) Method for Ewald Sums in Large Systems. *J. Chem. Phys.* **1993**, *98* (12), 10089–10092.

(69) Steinbach, P. J.; Brooks, B. R. New Spherical-Cutoff Methods for Long-Range Forces in Macromolecular Simulation. *J. Comput. Chem.* **1994**, *15* (7), 667–683.

(70) Virtanen, P.; Gommers, R.; Oliphant, T. E.; Haberland, M.; Reddy, T.; Cournapeau, D.; Burovski, E.; Peterson, P.; Weckesser, W.; Bright, J.; van der Walt, S. J.; Brett, M.; Wilson, J.; Millman, K. J.; Mayorov, N.; Nelson, A. R. J.; Jones, E.; Kern, R.; Larson, E.; Carey, C. J.; Polat, İ.; Feng, Y.; Moore, E. W.; VanderPlas, J.; Laxalde, D.; Perktold, J.; Cimrman, R.; Henriksen, I.; Quintero, E. A.; Harris, C. R.; Archibald, A. M.; Ribeiro, A. H.; Pedregosa, F.; van Mulbregt, P.; SciPy 1.0 Contributors. SciPy 1.0: Fundamental Algorithms for Scientific Computing in Python. *Nat. Methods* **2020**, *17* (3), 261–272.

(71) *Jaxopt: Hardware Accelerated, Batchable and Differentiable Optimizers in JAX*; Github.

(72) Frisch, M. J.; Trucks, G. W.; Schlegel, H. B.; Scuseria, G. E.; Robb, M. A.; Cheeseman, J. R.; Scalmani, G.; Barone, V.; Petersson, G. A.; Nakatsuji, H.; Others. Gaussian 16 REvision C.01. 2016.

(73) Wang, J.; Wang, W.; Kollman, P. A.; Case, D. A. Automatic Atom Type and Bond Type Perception in Molecular Mechanical Calculations. *J. Mol. Graph. Model.* **2006**, *25* (2), 247–260.

(74) Jewett, A. I.; Stelter, D.; Lambert, J.; Saladi, S. M.; Roscioni, O. M.; Ricci, M.; Autin, L.; Maritan, M.; Bashusqeh, S. M.; Keyes, T.; Dame, R. T.; Shea, J.-E.; Jensen, G. J.; Goodsell, D. S. Moltemplate: A Tool for Coarse-Grained Modeling of Complex Biological Matter and Soft Condensed Matter Physics. *J. Mol. Biol.* **2021**, *433* (11), 166841.

(75) Yoneya, M.; Kawasaki, M.; Ando, M. Molecular Dynamics Simulations of Pentacene Thin Films: The Effect of Surface on Polymorph Selection. *J. Mater. Chem.* **2010**, *20* (46), 10397–10402.

(76) Friederich, P.; Meded, V.; Poschlad, A.; Neumann, T.; Rodin, V.; Stehr, V.; Symalla, F.; Danilov, D.; Lüdemann, G.; Fink, R. F.; Kondov, I.; von Wrochem, F.; Wenzel, W.

Molecular Origin of the Charge Carrier Mobility in Small Molecule Organic Semiconductors. *Adv. Funct. Mater.* **2016**, *26* (31), 5757–5763.

(77) Nishi, T.; Kanno, M.; Kuribayashi, M.; Nishida, Y.; Hattori, S.; Kobayashi, H.; von Wrochem, F.; Rodin, V.; Nelles, G.; Tomiya, S. Impact of Molecular Orientation on Energy Level Alignment at C60/Pentacene Interfaces. *Appl. Phys. Lett.* **2018**, *113* (16), 163302.